

Ultrafast Parallel LiDAR with Time-encoding and Spectral Scanning: Breaking the Time-of-flight Limit

Zihan Zang

Tsinghua University

Zhi Li

Tsinghua University

Yi Luo

Tsinghua University

Yan-Jun Han

Tsinghua National Laboratory for Information Science and Technology, Tsinghua University

Xuanyi Liu

Tsinghua University

H.Y. Fu (✉ hyfu@sz.tsinghua.edu.cn)

Tsinghua University

Article

Keywords:

Posted Date: April 2nd, 2021

DOI: <https://doi.org/10.21203/rs.3.rs-311503/v1>

License:  This work is licensed under a Creative Commons Attribution 4.0 International License.

[Read Full License](#)

Ultrafast Parallel LiDAR with Time-encoding and Spectral Scanning: Breaking the Time-of-flight Limit

Zihan Zang^{1,†}, Zhi Li^{1,†}, Yi Luo^{2,3,4,*}, Yanjun Han^{2,3,4,*}, Xuanyi Liu¹, & H.Y. Fu^{1,*}

¹Tsinghua Shenzhen International Graduate School (Tsinghua SIGS), Tsinghua University, Shenzhen 518055, China.

²Beijing National Research Center for Information Science and Technology (BNRist), Department of Electronic Engineering, Tsinghua University, Beijing, 100084, China.

³Flexible Intelligent Optoelectronic Device and Technology Center, Institute of Flexible Electronics Technology of THU, Zhejiang, Jiaxing, 314006, China.

⁴Center for Flexible Electronics Technology, Tsinghua University, Beijing, 100084, China.

[†]Equal contribution authors

*E-mail: luoy@tsinghua.edu.cn, hyfu@sz.tsinghua.edu.cn

(Date 3/9/2021)

Abstract

Light detection and ranging (LiDAR) has been widely used in autonomous driving and large-scale manufacturing. Although state-of-the-art scanning LiDAR can perform long-range three-dimensional imaging, the frame rate is limited by both round-trip delay and the beam steering speed, hindering the development of high-speed autonomous vehicles. For hundred-meter level ranging applications, a several-time speedup is highly desirable. Here, we uniquely combine fiber-based encoders with wavelength-division multiplexing devices to implement all-optical time-encoding on the illumination light. Using this method, parallel detection and fast inertia-free spectral scanning can be achieved simultaneously with single-pixel detection. As a result, the frame rate of a scanning LiDAR can be multiplied with scalability. We demonstrate a 4.4-fold speedup for a maximum 75-m detection range, compared with a time-of-flight-limited laser ranging system. This approach has the potential to improve the velocity of LiDAR-based autonomous vehicles to the regime of hundred kilometers per hour and open up a new paradigm for ultrafast-frame-rate LiDAR imaging.

28 Introduction

29 To obtain the three-dimensional depth information of a long-range object, time-of-flight (TOF) imaging
30 is one of the most powerful methods with high accuracy and high transverse spatial resolution. TOF
31 imaging-based light detection and ranging (LiDAR) has been widely used in industrial automation¹,
32 logistics², autonomous driving³, robotics⁴ and airborne remote sensing⁵, etc. For these applications, the
33 acquisition time is crucial, because fast-changing scenes and fast-moving objects require a high image
34 refresh rate to perform data post-processing such as object identification, tracking and measurement.

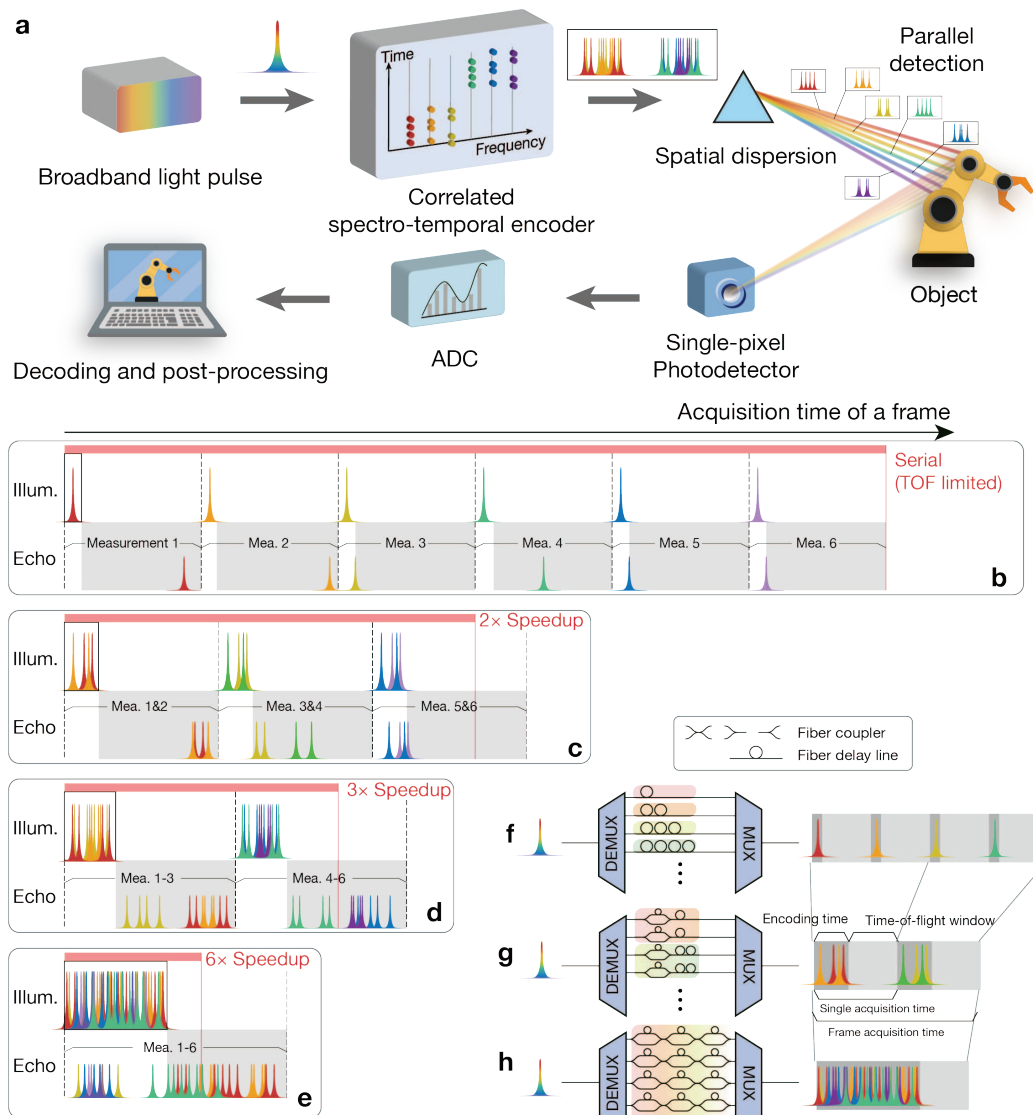
35 The acquisition time of a scanning LiDAR is determined by two factors: the speed of beam scanning and
36 the maximum time of flight. For most commercial LiDARs, the speed of beam scanning is one of the
37 main bottlenecks. Mechanically scanning LiDARs suffer from slow scanning rate of several kHz. State-
38 of-the-art optical phased array (OPA) technology has the potential of MHz-to-GHz scanning rate, but the
39 large-scale integration of low-loss active optical antennas is difficult to achieve, and the high peak optical
40 power requirement of TOF imaging is hard to fulfill with current photonic integration platforms. Spectral
41 scanning using a spatially dispersive element and a broadband source is another promising method to
42 achieve uniquely high speed, which is inherently inertia-free and compact. Recently, spectral beam
43 scanning with near-THz scanning rate has been reported⁶. Microscopy^{7,8}, endoscopy⁹, photography¹⁰ and
44 LiDAR^{11,12} based on spectral scanning have been demonstrated with record frame rates.

45 As the pursuit of rapid beam-steering method pushes up the speed of current LiDAR, the time
46 consumption of round-trip delay of light pulses becomes increasingly remarkable. Next-generation high-
47 speed autonomous vehicles such as unmanned aerial vehicle (UAV) push or exceed the so-called time-
48 of-flight limit. For example, to resolve a movement of 0.1 m, which is the baseline depth resolution of
49 most TOF imaging systems, an autonomous vehicle with a speed of 100 km/h and at a distance of 100 m
50 requires an acquisition rate higher than 5.6 MHz to generate a normal 3D image with 100 lines and 200
51 pixels per line. However, a TOF limited ranging system can only offer a detection rate up to 1.5 MHz
52 for a detection range of 100 m. Thus, a few times of speed improvement beyond TOF limit is critical.
53 TOF limit is mainly due to the serial detection mode of a scanning LiDAR and can be alleviated by
54 introducing parallelism. The most direct approach to implement parallelism is the use of pixelated arrays,

55 which can eliminate the need of beam scanning. However, high-resolution, long-range LiDAR based on
56 TOF imaging preferred by industrial automation and autonomous driving requires high-speed and highly
57 sensitive photodetectors with bandwidth of tens of GHz and corresponding high-speed sampling circuits.
58 However, it is difficult to realize large-scale integration for such detector arrays. Recently, parallel
59 coherent LiDAR was demonstrated using a soliton microcomb¹². With heterodyne detection, detectors
60 with relatively low bandwidth can be applied. Nevertheless, to obtain high spatial resolution, large-scale
61 integration of many high-performance detectors is still needed. Therefore, it is highly desirable to find a
62 method to implement parallelism for LiDARs using a single-pixel detector. Compressive sensing-based
63 LiDAR with a pixelated spatial modulator can achieve parallel detection with a single detector^{13,14,15}.
64 However, the need of multiple measurements, high computational complexity and the speed of spatial
65 modulators slow down the actual speed. Temporal encoding is another method to implement parallelism
66 with a single receiver. Temporal encoded imaging systems based on electro-optic modulation¹⁷⁻¹⁹ or
67 optical feedback²⁰ enables parallelism and thus reduce the acquisition time, but the speed limitations
68 caused by mechanical beam scanning devices and modulators make it impractical to surpass the time-of-
69 flight-limited speed.

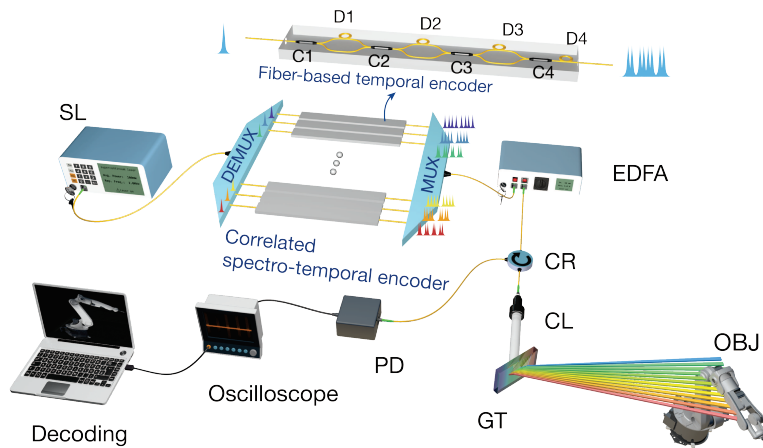
70 Here, we demonstrate a parallelism technique to enable scalable speed improvement beyond time-of-
71 flight limit for a single-pixel scanning LiDAR, and fast spectral scanning is incorporated to offer an
72 unlimited inertia-free beam scanning. As shown in Fig. 1a, by employing a fiber-based all-optical
73 temporal encoder in each wavelength multiplexed channel, optical code division multiplexing (OCDM)
74 is implemented to achieve parallelism. Key to our approach is the generation and leverage of a correlated
75 spectro-temporal modulation with high degree of freedom (DOF). In comparison, previous spectro-
76 temporal encoded imaging systems^{10,16} use a serial time-encoding strategy (Figs. 1b and 1f). As the
77 dispersive elements perform a one-to-one spectrum-to-space mapping, only serial detection can be
78 achieved, and the imaging speed is TOF limited. Using the proposed approach, we exploit correlations
79 between the spectral and temporal DOFs to enable parallel TOF ranging for the first time, leading to
80 multiplication of detection speed. It is also worth noting that high-DOF spectro-temporal modulation has
81 recently been employed in parallel optical computing^{21,22}. The speed multiplier effect of our proposed
82 system relies on the temporal code size. A set of temporal code with N types of code words can generate
83 M parallel channels and thus reduces the acquisition time of a frame (Figs. 1b-1e). Note that the final

84 multiplier is slightly less than M because of the additional cost of encoding time. Moreover, benefiting
 85 from programmable all-optical fiber-based encoders²³, the scale of the speed multiplication is
 86 reconfigurable. A partially correlated spectro-temporal encoder (Fig. 1g) with a simpler structure offers
 87 a smaller multiplier (Figs. 1c and 1d) while a fully correlated spectro-temporal encoder (Fig. 1h) enables
 88 single-shot detection (Fig. 1e) at the cost of complexity. By implementing partially correlated spectro-
 89 temporal encoders on 45 distinct wavelength channels, we generate 5 parallel OCDM channels with
 90 optical orthogonal code (OOC)²⁴⁻²⁶, thus reducing the number of measurements from 45 to 8. For ranging
 91 distance of 75 and 25 meters, we achieve 4.4 and 3.6 times the time-of-flight-limited speed, respectively.
 92 The proposed parallelism approach can enable ultrafast long-range scanning LiDAR much faster than
 93 the time-of-flight-limited speed, which is highly desirable for the aforementioned applications.



95 **Figure 1 | All-optical correlated spectro-temporal encoding enables scalable speedup of LiDAR beyond**
 96 **time-of flight limit. a**, a correlated spectro-temporal encoder modulates the input broadband light pulse. A
 97 dispersive element performs the spectrum-to-space mapping and thus achieve spectral beam scanning.
 98 Meanwhile, parallel ranging by a single-pixel detector is achieved by temporal encoding and decoding. **b**,
 99 illumination and echo signal of a serial spectro-temporal encoded LiDAR, which is time-of-flight limited.
 100 Because of the lack of parallelism, 6 scan periods are required for a frame with 6 ranging points. **c-e**,
 101 illumination and echo signals of correlated spectro-temporal encoded LiDAR proposed here. Spectro-temporal
 102 encoding with different degree of correlation enables parallelism and speeds up the LiDAR beyond time-of-
 103 flight limit. The final speedup multiplier is slightly less than parallelism multiplier because of the additional
 104 cost of encoding time. **f**, a serial spectro-temporal encoder used by **b**, where different delays are introduced for
 105 different spectral channels. **g**, a partially correlated spectro-temporal encoder used by **c** and **d**, where spectral
 106 channels are divided into several groups, and different groups share the same set of optical orthogonal code
 107 but different global delay. The channels within a group will operate parallelly. **h**, a fully correlated spectro-
 108 temporal encoder used by **e**, where a set of optical orthogonal code is applied to all spectral channels, and all
 109 channels will operate in parallel.

110 Results



111

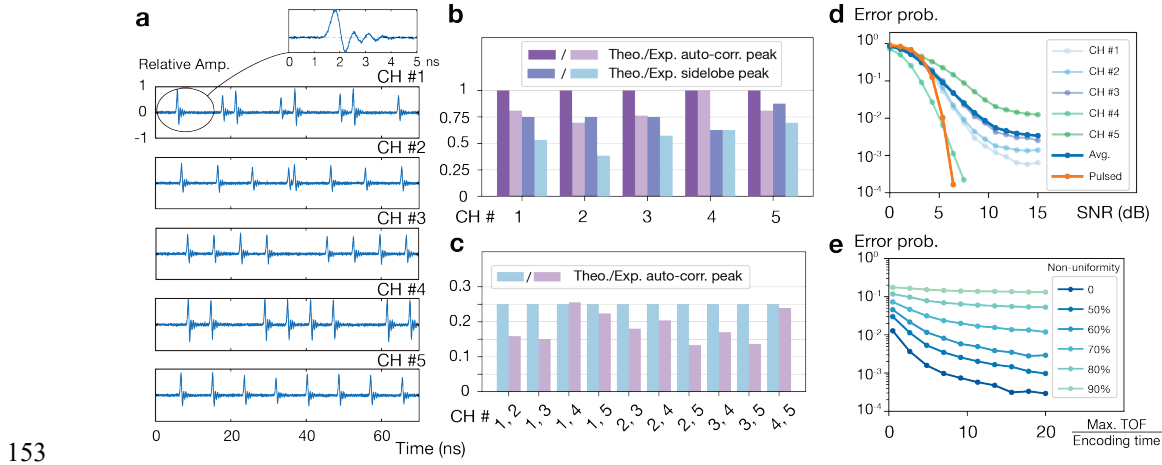
112 **Figure 2 | Experimental setup.** A wavelength division demultiplexer (DEMUX) splits the input broadband
 113 light pulse generated by a supercontinuum laser (SL) into multiple spectral channels. A fiber-based encoder
 114 array performs temporal encoding for each channel, and all the channels are combined by a wavelength division
 115 multiplexer (MUX). A correlated spectro-temporal encoded light pulse train is thus generated and transmitted

116 for spectral scanning and time-of-flight ranging. A diffraction grating (GT) performs horizontal spectral
117 scanning; vertical scanning is implemented mechanically using a rotatable mirror (not shown in figure). The
118 echo light from the object is received by a photodetector and the temporal encoding is sampled and decoded
119 by post-processing. C1-C4, fiber couplers; D1-D4, fiber delay lines; EDFA, Erbium-Doped Fiber Amplifier;
120 CR, optical circulator; CL, collimator; PD, photodetector; ADC, analog-to-digital convertor.

121 **Experimental setup:** As shown in Fig. 2, a gain-switched supercontinuum laser with an optical filter
122 covering 1540-1560 nm provides broadband light pulses with a width of 100 ps and variable repetition
123 frequency. Each light pulse is spectro-temporally modulated with high DOF by a fiber-optic encoder,
124 which will be described below. The modulated pulse is then amplified by an erbium-doped fiber amplifier
125 (EDFA) and transmitted through a collimator. Spectral scanning is achieved by a diffraction grating. The
126 echo light is collected by the same optics, redirected by an optical circulator and received by a high-
127 speed APD (1.5-GHz bandwidth, linear mode). The echo signal from the detector is sampled and
128 captured by a high-speed oscilloscope (Tektronix MSO72304DX, 33GHz) and decoded via post-
129 processing hardware.

130 **Correlated spectro-temporal encoding:** The correlated spectro-temporal encoder (see Fig. 2) is
131 comprised of two arrayed waveguide gratings (AWGs), and a series of homemade fiber-based temporal
132 encoders. AWGs are used as wavelength multiplexer and demultiplexer to generate 45 distinct spectral
133 channels. Considering the complexity of the fiber-based temporal encoder, a partially correlated spectro-
134 temporal encoder similar to Fig. 1g is chosen, where 45 spectral channels are divided into 8 groups. Each
135 group contains 5 parallel OCDM channels, each of which contains an encoder with 4 fiber couplers (C1-
136 C4 in Fig. 2) and 3 fiber delay lines (D1-D3 in Fig. 2). The encoder is able to generate 5 kinds of OOCs
137 by adjusting the delays. All generated OOCs has a whole code length (length of the binary sequence) of
138 56, which contains 8 non-zero bits. The time slot (the minimum encoding temporal interval) is chosen as
139 1.2 ns, according to the available bandwidth of the photodetector. Therefore, the total encoding time t_{code}
140 of the OOC is 67.2 ns. The encoding result of one of the parallel groups is shown in Fig. 3a. Other details
141 of the construction of OOCs can be found in the Methods and Supplementary Information. As each group
142 shares the same set of OOCs, incremental global time delays (D4 in Fig. 2) are introduced for different
143 groups to separate them in the time domain, which is similar to the time-stretch technique¹¹. The

144 increment of the global delay T_d corresponds to a single acquisition cycle, which equals to the sum of the
 145 encoding time t_c and the time-of-flight window τ for the maximum range without ambiguity (see Figs.
 146 1f-h). T_d is set to be 167 ns for 25-m maximum detection range and 500 ns for 75-m case, respectively.
 147 Thus, for a frame with N effective ranging pixels, M parallel channels for each group, and thus N/M
 148 groups, the total acquisition time T for a frame is given by $N(t_c + \tau)/M$, which is also the repetition period
 149 that the laser source should be configured. Compared with a serially scanning LiDAR with a total
 150 acquisition time $N\tau$, the multiplier of speed improvement is $M/(1+t_c/\tau)$, which increasingly approaches
 151 M as t_c/τ decreases, i.e., the encoding time becomes unremarkable compared with the time-of-flight
 152 window.

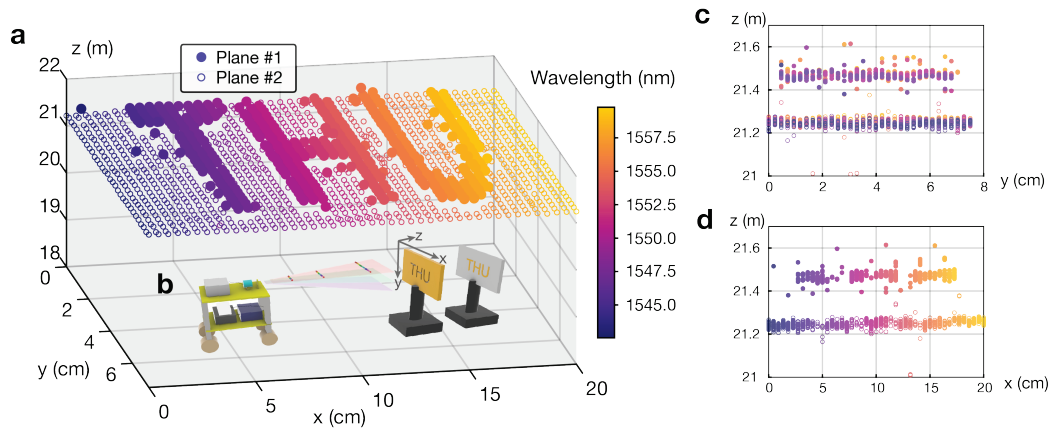


154 **Figure 3 | Encoding and decoding performance.** **a**, encoding waveform of 5 OCDM channels belonging to
 155 one of the groups, captured by a photodetector with 1.5-GHz bandwidth; a single pulse is zoomed in. **b**,
 156 theoretical and experimental results of normalized auto-correlation main peak value λ_p and maximum auto-
 157 correlation sidelobe peak λ_a of each OCDM channel. **c**, theoretical and experimental results of normalized
 158 cross-correlation peak value λ_c between each two different OCDM channels. **d**, error probability under
 159 different signal-to-noise ratio, estimated by Monte Carlo analysis with 5×10^4 simulations for each point. The
 160 results of 5 OCDM channels and the averaged result are shown. For comparison, error probability of a pulsed
 161 LiDAR is also provided. **e**, error probability under different detection time-of-flight window (i.e., maximum
 162 time of flight, normalized by the encoding time) and intensity non-uniformity among different channels
 163 (without additional noise, and thus showing the impact of MAI), estimated by Monte Carlo analysis with 5×10^4
 164 simulations for each point.

165 **Temporal decoding results:** It is possible that the echo light belonging to the same parallel group arrive
166 at the same time or overlap with each other, and the arriving order is also uncertain. To identify the exact
167 time of flight of a specific channel, temporal decoding is needed. Temporal decoding is achieved by
168 correlating the sampled echo signal $e(t)$ with each OOC codeword $c_i(t)$, i.e. $\langle e, c_i \rangle = \int e(t' - t)c_i(t')dt'$,
169 which can be calculated efficiently and parallelly with current hardware^{27,28}. Due to the orthogonality of
170 OOCs, the auto-correlation signal exhibits a high peak value, whose position corresponding to the
171 arriving time of the codeword, while the cross-correlation signals corresponding to other OCDM
172 channels show low peak values. Cross-correlation signals and the sidelobe of auto-correlation signal
173 would lead to decoding noise, which is denoted as multiple access interference (MAI). An ideal OOC set
174 $\{c_i\}$ with low-level MAI consists of white-noise-like codewords with good orthogonality and
175 randomness. Orthogonality can be evaluated by the maximum value λ_c of the cross-correlation between
176 different codewords $\langle c_i, c_j \rangle$ ($i \neq j$), which approaches zero in the ideal case. Randomness can be
177 evaluated by the maximum value λ_a of auto-correlation sidelobes of each codeword $\langle c_i, c_i \rangle$, which also
178 approaches zero in the ideal case. Normalized λ_c and λ_a of one of the OCDM group calculated both from
179 codebook and experimentally captured waveform are shown in Figs. 3b and 3c. The height of the
180 normalized auto-correlation main peak λ_p is also depicted in Fig. 3b, which reflects the relative intensity
181 differences among OCDM channels. The difference between theoretical and experimental results is
182 mainly due to the fiber length error for fixed fiber delay lines and slight differences in the loss and
183 coupling of the fiber-optic devices.

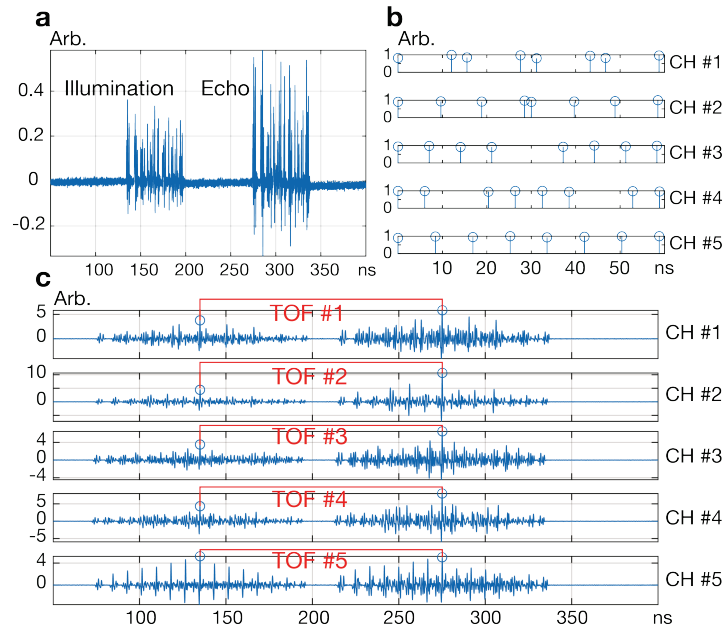
184 To assess the impact of MAI, error probability of this OCDM LiDAR is estimated by Monte Carlo
185 simulation, using the experimentally captured waveforms. Figure 3d shows the error probability under
186 different noise level. Compared to conventional pulsed LiDARs, the total noise of this LiDAR includes
187 not only the detection noise but also the MAI. As a result, the signal-to-noise ratio (SNR) requirement
188 for high-fidelity detection is higher for an OCDM LiDAR. Figure 3e shows the error probability induced
189 by MAI (without additional noise). As MAI only exists when two or more codewords overlaps, which is
190 called a collision, a longer detection temporal window (compared with the encoding time of a codeword)
191 can alleviate the impact of MAI. On the other hand, intensity non-uniformity among different OCDM
192 channels will exacerbate the MAI, because cross-correlation peaks formed by a strong channel may
193 exceed the auto-correlation peak from a weak channel. In addition, the OOC coding selection also

194 determines the magnitude of the MAI. In other words, the cost of parallelism here achieved by OCDM
 195 is a slight reduction in the signal-to-noise ratio caused by MAI.



196

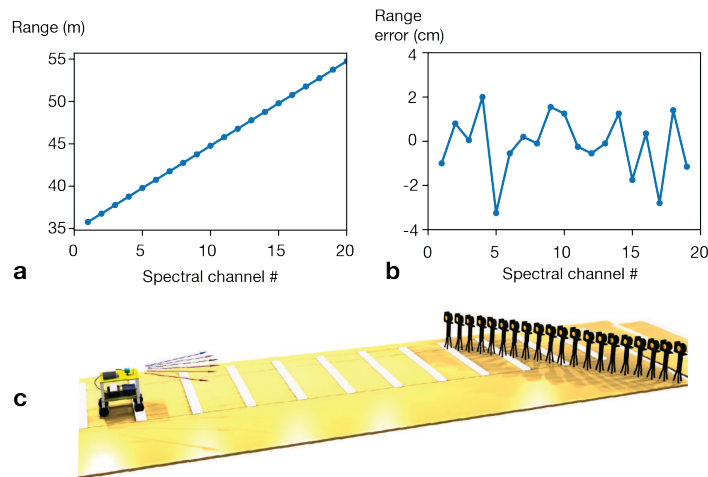
197 **Figure 4 | 3D Imaging result.** **a**, 3D image of the two targets with Tsinghua University logo (THU). The two
 198 targets are positioned 6.5 m away. The result contains a 14.8-m effective length of fiber link. Spectral scanning
 199 generates 45 channels along horizontal axis (y). Vertical scan is performed by a rotatable mirror. Large circles
 200 indicate the front target (plane #1) and small circles indicate the back target (plane #2). **b**, experimental set-up.
 201 **c**, projection of the 3D image along the x axis. **d**, projection of the 3D image along the y axis.



202

203 **Figure 5 | Decoding result.** **a**, sampled echo signal of a parallel group including 5 OCDM channels. **b**,
 204 temporal waveform of the 5 OOC codewords. Intensity fluctuations due to fiber optic encoders are incorporated.
 205 **c**, after correlating the echo signal with the 5 OOCs, 5 decoded signals are obtained. Two marked auto-
 206 correlation peaks in each decoded channel indicate the transmission time of detection light and the arriving
 207 time of echo, respectively.

208 **Imaging performance:** To demonstrate 3D imaging performance of the proposed LiDAR, targets are
 209 set as two pieces of cardboards spaced by 0.5 m, one of which is hollowed out in the shape of Tsinghua
 210 University logo (see Fig. 4b). 45 spectral channels spanning from 1540 nm to 1560 nm are dispersed by
 211 a diffraction grating with a line density of 800 line/mm, realizing horizontal line scan with a field of view
 212 (FOV) of 2° and covering the logo with a width of 20 cm. The vertical scan is performed mechanically
 213 using a rotatable mirror. The maximum detection range is chosen as 25 m, corresponding to a maximum
 214 detection rate of 6 MHz for a time-of-flight limited serially scanning LiDAR. By using the 5-channel
 215 OCDM, a maximum detection rate of 21.8 MHz is achieved, leading to 3.6-fold speedup beyond time-
 216 of-flight limit. The sampled echo signal of a parallel 5-channel group is shown in Fig. 6a. After correlated
 217 with 5 OOCs shown in Fig. 6b, the decoded signals of 5 channels are obtained, as illustrated in Fig. 6c.
 218 Despite the appearance of MAI sidelobes, two main auto-correlation peak stands out prominently in each
 219 decoded signal, which indicates the arriving time of illumination and echo signal belonging to each
 220 channel, respectively. As a result, the time-of-flight results of the 5 parallel channels can be obtained
 221 during a single detection cycle. The imaging result is depicted in Figs. 4a, 4c and 4d, in which both
 222 target planes are clearly captured.

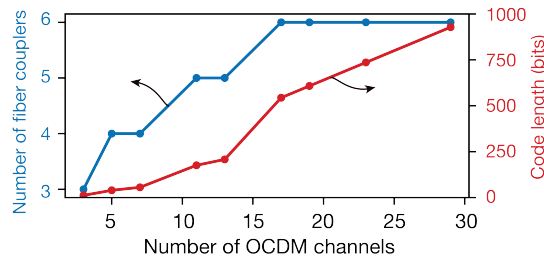


223

224 **Figure 6 | Long-range detection result. a**, ranging result of 20 spectral channels. The targets are 20 poles
 225 with reflective tags and placed at a range from 21 m to 40 m. The result contains a 14.8-m effective length of
 226 fiber link. They are equidistant from each other at a distance of 1 m. **b**, ranging error of the distance between
 227 each adjacent pole, which exhibits a depth resolution of several centimeters. **c**, experimental setup.

228 **Long-range performance:** One advantage of the parallel LiDAR is the ability to perform high-speed
 229 long-range imaging. We constructed a long-range 3D scene containing 20 poles with reflective tags (see
 230 Fig. 6c). Only horizontal spectral scanning is performed, where 20 out of 45 spectral channels are selected
 231 and divided into 4 groups, each containing 5 OCDM parallel channels. Another diffraction grating with
 232 a line density of 1200 line/mm is used to achieve a FOV of 3.8°. The maximum detection range is set as
 233 75 m, corresponding to a maximum detection rate of 2 MHz for a time-of-flight limited serially scanning
 234 LiDAR. With parallelism, detection rate is increased to 8.8 MHz, indicating 4.4 times the time-of-flight
 235 limited speed. The accuracy performance is depicted in Figs. 6a and 6b, confirming accurate range
 236 mapping even for relatively long-range situation.

237 Discussion



238

239 **Figure 7 | Scalability of OCDM channels using quasi-prime code.** As the number of OCDM channels
 240 increases, the scale of parallelism increases but code length and the required number of optical couplers per
 241 channel increases as well.

242 The speedup scalability of the proposed LiDAR mainly depends on the number of channels M within an
 243 OCDM group. However, large parallel channels M has two main drawbacks, i.e., the increase of code
 244 length and the number of required optical couplers in fiber-optic encoder, which is depicted in Fig. 7 for
 245 the case of quasi-prime code. The increase of code length or encoding time will reduce actual multiplier

246 of speed improvement because of the time consumption of code transmission, and the large number of
247 fiber couplers will increase system complexity. To address the limitation of scalability, it is possible to
248 reduce the encoding time by implementing a smaller time slot. In our experiment, the minimum time slot
249 is limited by the 1.5-GHz detector bandwidth. If a detector with higher speed is used, such as a 40-GHz
250 detector, the encoding time can be largely reduced and thus leads to better speedup effectiveness.
251 Benefiting from the single-pixel architecture in this system, such high-speed detectors are practical to
252 employ. Furthermore, if high-speed electro-optical modulators are used in place of fiber-optic encoders
253 for OCDM code generation, OOCs other than quasi-prime code and with shorter code length can be
254 adopted, which not only extends the scalability of the system, but also helps improve the system
255 performance due to the reduced MAI.

256 Another potential issue of the proposed system is the reduced peak illumination power caused by
257 temporal encoding. This effect becomes more notable as the number of non-zero bits in codeword
258 increases, which also limits the scalability of the system. When code weight (the number of non-zero
259 bits) equals to Q , the peak power becomes $1/Q$ of the unmodulated case. For the case of quasi-prime
260 code, Q equals to 2^L where L is the number of fiber couplers, and thus the impact on scalability can also
261 be seen in Fig. 7. During the correlation process, signal peaks corresponding to non-zero bits are
262 constructively added back to the unmodulated case, whereas thermal noise (assumed to be Gaussian) is
263 incoherently added and become \sqrt{Q} times of the unmodulated case. As a result, effective illumination
264 power reduction of the system is $1/\sqrt{Q}$ when compared to a single-pulsed LiDAR. Nevertheless, this
265 reduction effect does not take into account the presence of subsequent EDFAs. The insertion of a simple
266 pre-amplifier will effectively compensate the loss of illumination power²⁹. Besides, as the fiber-based
267 temporal encoder only replicates input pulses according to quasi-prime code (see Methods), the generated
268 pulses with nearly identical pulse width with input pulses are relatively evenly distributed, which is
269 beneficial to pulse amplification.

270 In conclusion, we propose and demonstrate a method to implement parallelism for single-pixel scanning
271 LiDARs. Scalable parallelism and rapid spectral scanning are achieved simultaneously by correlated
272 spectro-temporal modulation using all-optical fiber-optic encoders and a dispersive element. A line scan
273 rate of several hundreds of kilohertz can be achieved even for tens of meters of detection range, breaking

274 the time-of-flight limit of serially scanning LiDARs. Our approach can enable next-generation high-
 275 speed autonomous vehicles and manufacturing with moving speed beyond hundred kilometers per hour.
 276 Also, this method can be further extended to other active imaging systems which uses serially scanning
 277 illumination, such as multiphoton microscopy⁸ and ultrafast imaging^{10,16}.

278 **Methods**

279 **OCDM encoding:** Quasi-prime code (QPC)²⁵ is employed to implement all-optical OCDM. The
 280 generation of QPC codeword set is as follows.

281 Firstly, choose a prime number P , and construct P sequences $\{S_i^P, i = 0 \text{ to } P - 1\}$, each with P elements.
 282 The j -th element of the i -th sequence is then given by

$$283 \quad S_i^P(j) = (i \cdot j) \bmod P, \text{ for } i = 0 \text{ to } P - 1; j = 0 \text{ to } P - 1.$$

284 Secondly, convert $\{S_i^P\}$ into P binary sequences $\{C_i^P, i = 0 \text{ to } P - 1\}$, each with P P -element frames, i.e.
 285 P^2 -element sequence. Each frame contains only one non-zero bit. The binary sequences are obtained
 286 using the following rules:

$$287 \quad C_i^P(n) = \begin{cases} 1, & \text{for } n = jP + S_i^P(j); j = 0 \text{ to } P - 1 \\ 0, & \text{otherwise.} \end{cases}$$

288 Thirdly, choose Q as the smallest power of two that is larger than P , and construct a new set of P^2
 289 sequences $\{C_{ik}^{QP}, i = 0 \text{ to } P - 1; k = 0 \text{ to } P - 1\}$, each with Q P -element frames, i.e. QP -element
 290 sequence. The n -th element of a sequence is given by

$$291 \quad C_{ik}^{QP}(n) = C_i^P((n + kP) \bmod P^2), \text{ for } n = 0 \text{ to } QP - 1.$$

292 Finally, the QPC set is generated by discarding nonsymmetric code from the set $\{C_{ik}^{QP}\}$. Each final QPC
 293 codeword is symmetric, with a code length of QP as well as code weight of Q .

294 **All-optical fiber-optic encoder:** An all-optical QPC encoder requires $\log_2 Q$ interferometers, which
295 contains $\log_2 Q + 1$ fiber couplers and $\log_2 Q$ fixed fiber delay lines to achieve a QPC codeword with
296 code weight of Q . The suitable delays can be easily found by checking non-zero bits in the codeword.
297 The details of the delay lines can be found in the Supplementary Information.

298 **Acknowledgements**

299 The authors would like to express sincere thanks to Tsinghua-Berkeley Shenzhen Institute (TBSI)
300 Faculty Start-up Fund.

301 **Author contributions**

302 Z. Z. and Z. L. proposed the idea, performed the experiments and designed the Monte Carlo simulations.
303 Z. Z., Z. L. and X.L. performed system analysis and prepared the laser source. H.F., Y.H., and Y.L.
304 contributed to the data analysis. Y.L. and H.F. supervised the research. All authors discussed the
305 manuscript together.

306 **Competing interests**

307 The authors declare no conflicts of interest.

308 **Data availability**

309 The data that support the findings of this study are available from the corresponding author upon
310 reasonable request.

311 **Reference**

- 312 1. Coffey, V. C. Integrated lidar: Transforming transportation. *Optics and Photonics News* 30, 40–47
313 (2019).

- 314 2. Schmitt, R. H. et al. Advances in Large-Scale Metrology – Review and future trends. *CIRP Annals*
315 65, 643–665 (2016).
- 316 3. LiDAR drives forwards. *Nat. Photon.* 12, 441–441 (2018).
- 317 4. Schwarz, B. Mapping the world in 3D. *Nat. Photon.* 4, 429–430 (2010).
- 318 5. Paynter, I. et al. Observing ecosystems with lightweight, rapid-scanning terrestrial lidar scanners.
319 *Remote Sens. Ecol. Conserv.* 2, 174–189 (2016).
- 320 6. Shaltout, A. M. et al. Spatiotemporal light control with frequency-gradient metasurfaces. *Science*
321 365, 374–377 (2019).
- 322 7. Hase, E. et al. Scan-less confocal phase imaging based on dual-comb microscopy. *Optica* 5, 634
323 (2018).
- 324 8. Karpf, S. et al. Spectro-temporal encoded multiphoton microscopy and fluorescence lifetime
325 imaging at kilohertz frame-rates. *Nat. Commun.* 11, 2062 (2020).
- 326 9. Yelin, D. et al. Spectral-domain spectrally-encoded endoscopy. *Opt. Express* 15, 2432 (2007).
- 327 10. Goda, K., Tsia, K. K. & Jalali, B. Serial time-encoded amplified imaging for real-time observation
328 of fast dynamic phenomena. *Nature* 458, 1145–1149 (2009).
- 329 11. Jiang, Y., Karpf, S. & Jalali, B. Time-stretch LiDAR as a spectrally scanned time-of-flight ranging
330 camera. *Nat. Photon.* 14, 14–18 (2020).
- 331 12. Riemensberger, J. et al. Massively parallel coherent laser ranging using a soliton microcomb. *Nature*
332 581, 164–170 (2020).
- 333 13. Howland, G. A., Lum, D. J., Ware, M. R. & Howell, J. C. Photon counting compressive depth
334 mapping. *Opt. Express* 21, 23822 (2013).
- 335 14. Li, F. et al. CS-ToF: High-resolution compressive time-of-flight imaging. *Opt. Express* 25, 31096
336 (2017).
- 337 15. Lum, D. J., Knarr, S. H. & Howell, J. C. Frequency-modulated continuous-wave LiDAR
338 compressive depth-mapping. *Opt. Express* 26, 15420 (2018).
- 339 16. Nakagawa, K. et al. Sequentially timed all-optical mapping photography (STAMP). *Nature Photon*
340 8, 695–700 (2014).
- 341 17. Kim, G. & Park, Y. LIDAR pulse coding for high resolution range imaging at improved refresh rate.
342 *Opt. Express* 24, 23810 (2016).
- 343 18. Fersch, T., Weigel, R. & Koelpin, A. A CDMA Modulation Technique for Automotive Time-of-
344 Flight LiDAR Systems. *IEEE Sensors J.* 17, 3507–3516 (2017).
- 345 19. Tsai, C.-M. & Liu, Y.-C. Anti-interference single-photon LiDAR using stochastic pulse position
346 modulation. *Opt. Lett.* 45, 439 (2020).
- 347 20. Cheng, C.-H. et al. 3D pulsed chaos lidar system. *Opt. Express* 26, 12230 (2018).
- 348 21. Xu, X. et al. 11 TOPS photonic convolutional accelerator for optical neural networks. *Nature* 589,
349 44–51 (2021).
- 350 22. Feldmann, J. et al. Parallel convolutional processing using an integrated photonic tensor core. *Nature*
351 589, 52–58 (2021).
- 352 23. Moslehi, B., Goodman, J. W., Tur, M. & Shaw, H. J. Fiber-optic lattice signal processing. *Proc.*
353 *IEEE* 72, 909–930 (1984).

- 354 24. Chung, F. R., Salehi, J. A. & Wei, V. K. Optical orthogonal codes: design, analysis and applications.
355 *IEEE Trans. Inf. Theory* **35**, 595–604 (1989).
- 356 25. Holmes, A. S. & Syms, R. R. All-optical CDMA using 'quasi-prime' codes. *J. Light. Technol.* **10**,
357 279–286 (1992).
- 358 26. Salehi, J. A. Code division multiple-access techniques in optical fiber networks. I. Fundamental
359 principles. *IEEE Trans. Commun.* **37**, 824–833 (1989).
- 360 27. McDonald, G. J., Ellis, J. S., Penney, R. W. & Price, R. W. Real-Time Vehicle Identification
361 Performance Using FPGA Correlator Hardware. *IEEE Trans. Intell. Transport. Syst.* **13**, 1891–1895
362 (2012).
- 363 28. Asif, M., Guo, X., Hu, A. & Miao, J. An FPGA-Based 1-GHz, 128×128 Cross-Correlator for
364 Aperture Synthesis Imaging. *IEEE Trans. VLSI Syst.* **28**, 129–141 (2020).
- 365 29. Pavlov, I., Ilbey, E., Dülgergil, E., Bayri, A. & Ilday, F. Ö. High-power high-repetition-rate single-
366 mode Er-Yb-doped fiber laser system. *Opt. Express* **20**, 9471–9475 (2012).

Figures

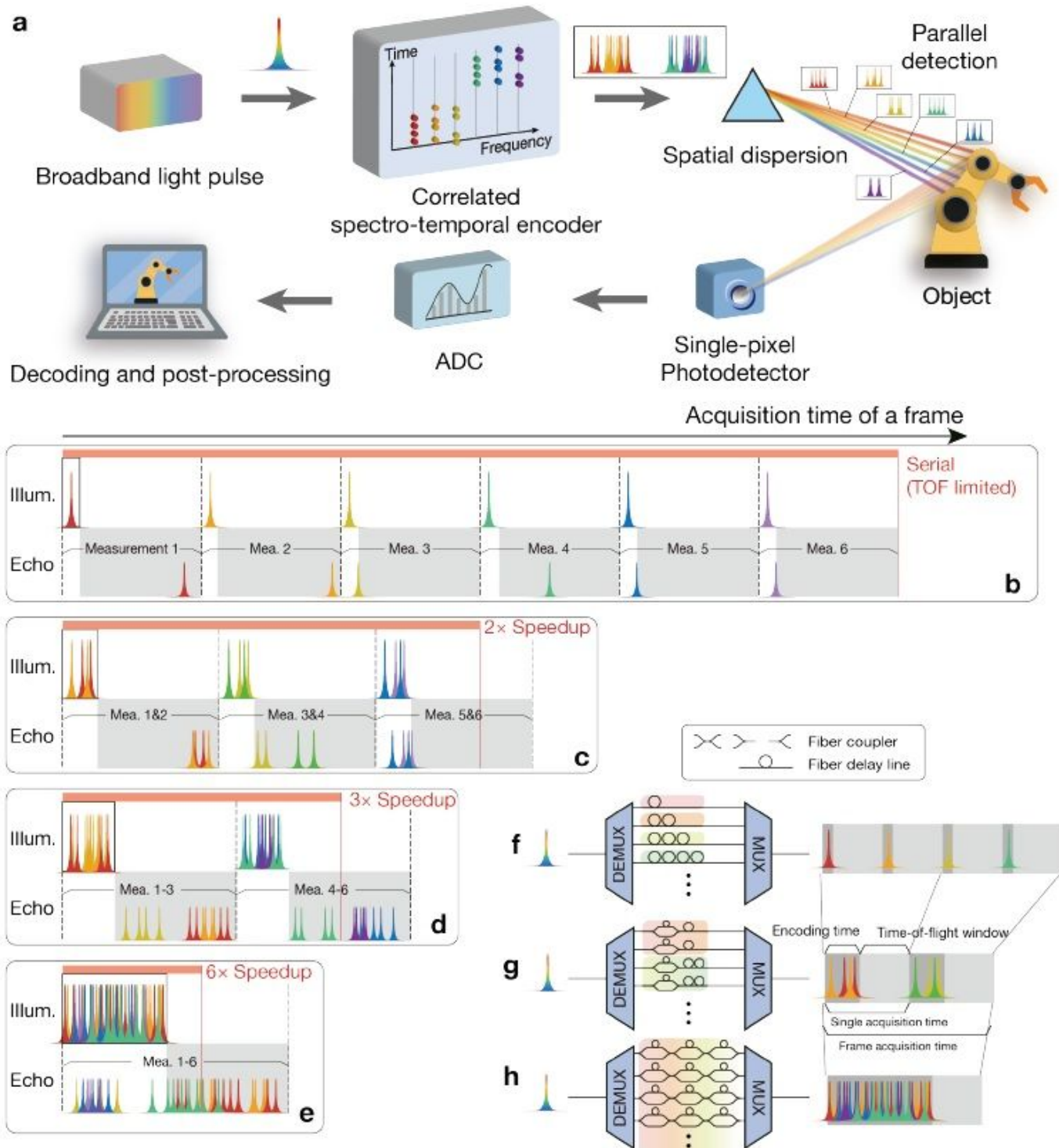


Figure 1

All-optical correlated spectro-temporal encoding enables scalable speedup of LiDAR beyond time-of flight limit. a, a correlated spectro-temporal encoder modulates the input broadband light pulse. A dispersive element performs the spectrum-to-space mapping and thus achieve spectral beam scanning. Meanwhile,

parallel ranging by a single-pixel detector is achieved by temporal encoding and decoding. b, illumination and echo signal of a serial spectro-temporal encoded LiDAR, which is time-of-flight limited. Because of the lack of parallelism, 6 scan periods are required for a frame with 6 ranging points. c-e, illumination and echo signals of correlated spectro-temporal encoded LiDAR proposed here. Spectro-temporal encoding with different degree of correlation enables parallelism and speeds up the LiDAR beyond time-of-flight limit. The final speedup multiplier is slightly less than parallelism multiplier because of the additional cost of encoding time. f, a serial spectro-temporal encoder used by b, where different delays are introduced for different spectral channels. g, a partially correlated spectro-temporal encoder used by c and d, where spectral channels are divided into several groups, and different groups share the same set of optical orthogonal code but different global delay. The channels within a group will operate parallelly. h, a fully correlated spectro-temporal encoder used by e, where a set of optical orthogonal code is applied to all spectral channels, and all channels will operate in parallel.

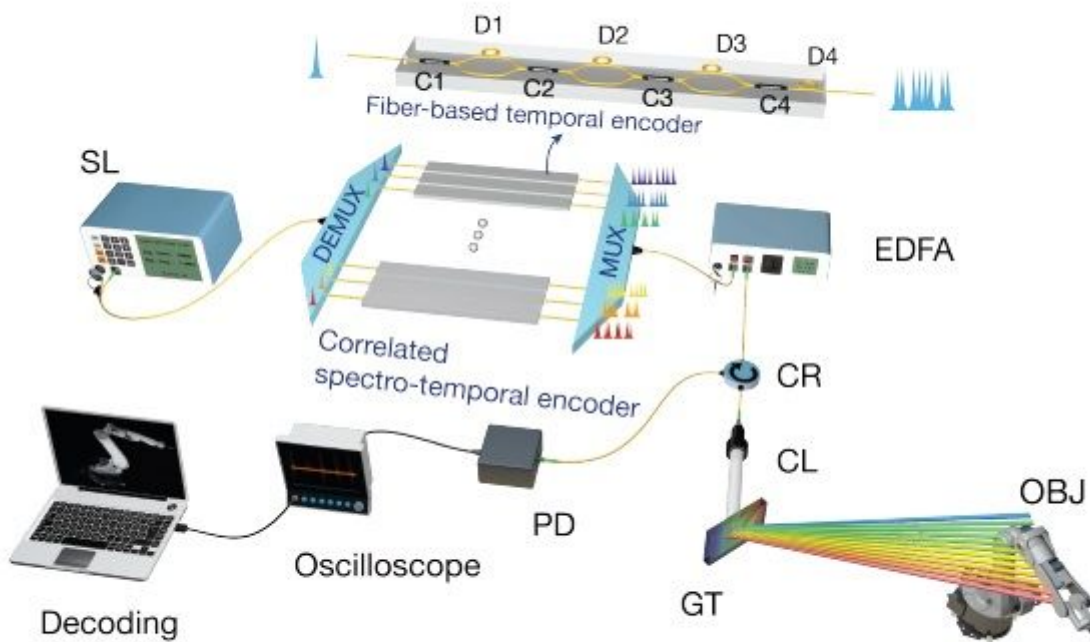


Figure 2

Experimental setup. A wavelength division demultiplexer (DEMUX) splits the input broadband light pulse generated by a supercontinuum laser (SL) into multiple spectral channels. A fiber-based encoder array performs temporal encoding for each channel, and all the channels are combined by a wavelength division multiplexer (MUX). A correlated spectro-temporal encoded light pulse train is thus generated and transmitted for spectral scanning and time-of-flight ranging. A diffraction grating (GT) performs horizontal spectral scanning; vertical scanning is implemented mechanically using a rotatable mirror (not shown in figure). The echo light from the object is received by a photodetector and the temporal encoding

is sampled and decoded by post-processing. C1-C4, fiber couplers; D1-D4, fiber delay lines; EDFA, Erbium-Doped Fiber Amplifier; CR, optical circulator; CL, collimator; PD, photodetector; ADC, analog-to-digital convertor.

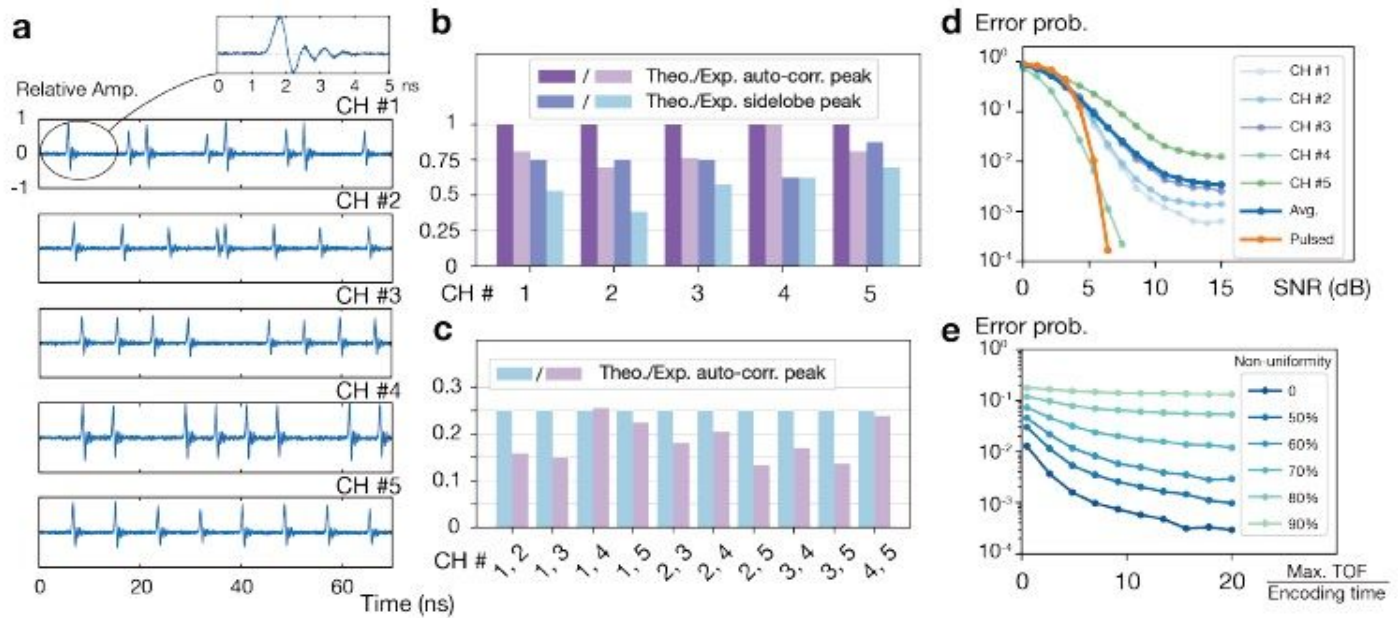


Figure 3

Encoding and decoding performance. a, encoding waveform of 5 OCDM channels belonging to one of the groups, captured by a photodetector with 1.5-GHz bandwidth; a single pulse is zoomed in. b, theoretical and experimental results of normalized auto-correlation main peak value λ_p and maximum auto-correlation sidelobe peak λ_a of each OCDM channel. c, theoretical and experimental results of normalized cross-correlation peak value λ_c between each two different OCDM channels. d, error probability under different signal-to-noise ratio, estimated by Monte Carlo analysis with 5×10^4 simulations for each point. The results of 5 OCDM channels and the averaged result are shown. For comparison, error probability of a pulsed LiDAR is also provided. e, error probability under different detection time-of-flight window (i.e., maximum time of flight, normalized by the encoding time) and intensity non-uniformity among different channels (without additional noise, and thus showing the impact of MAI), estimated by Monte Carlo analysis with 5×10^4 simulations for each point.

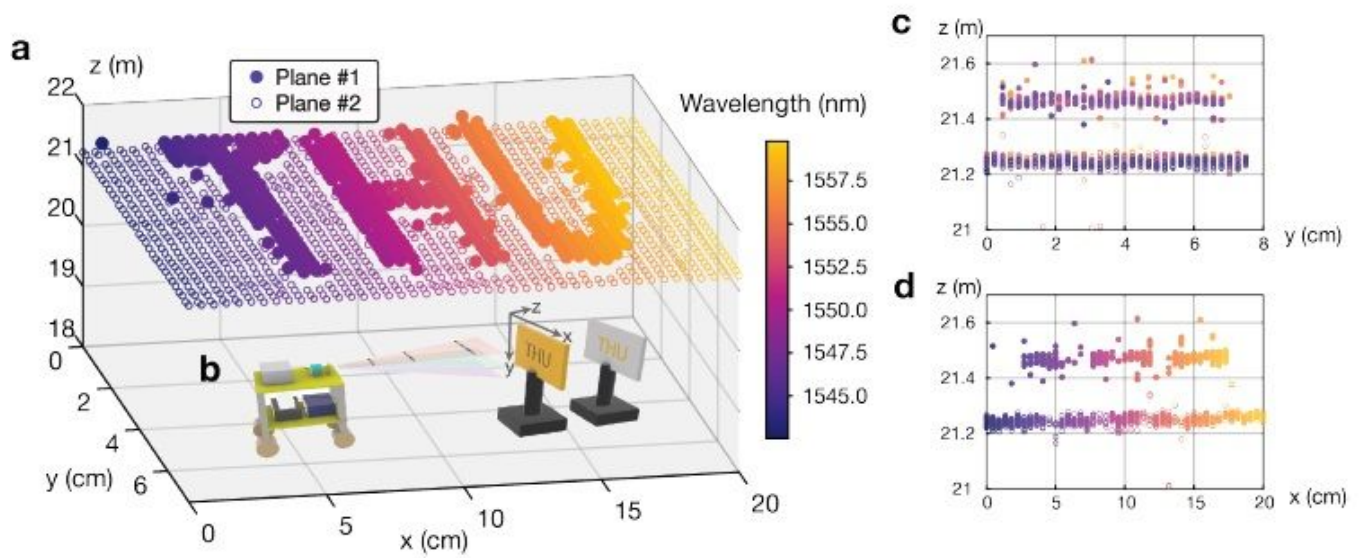


Figure 4

3D Imaging result. a, 3D image of the two targets with Tsinghua University logo (THU). The two targets are positioned 6.5 m away. The result contains a 14.8-m effective length of fiber link. Spectral scanning generates 45 channels along horizontal axis (y). Vertical scan is performed by a rotatable mirror. Large circles indicate the front target (plane #1) and small circles indicate the back target (plane #2). b, experimental set-up. c, projection of the 3D image along the x axis. d, projection of the 3D image along the y axis.

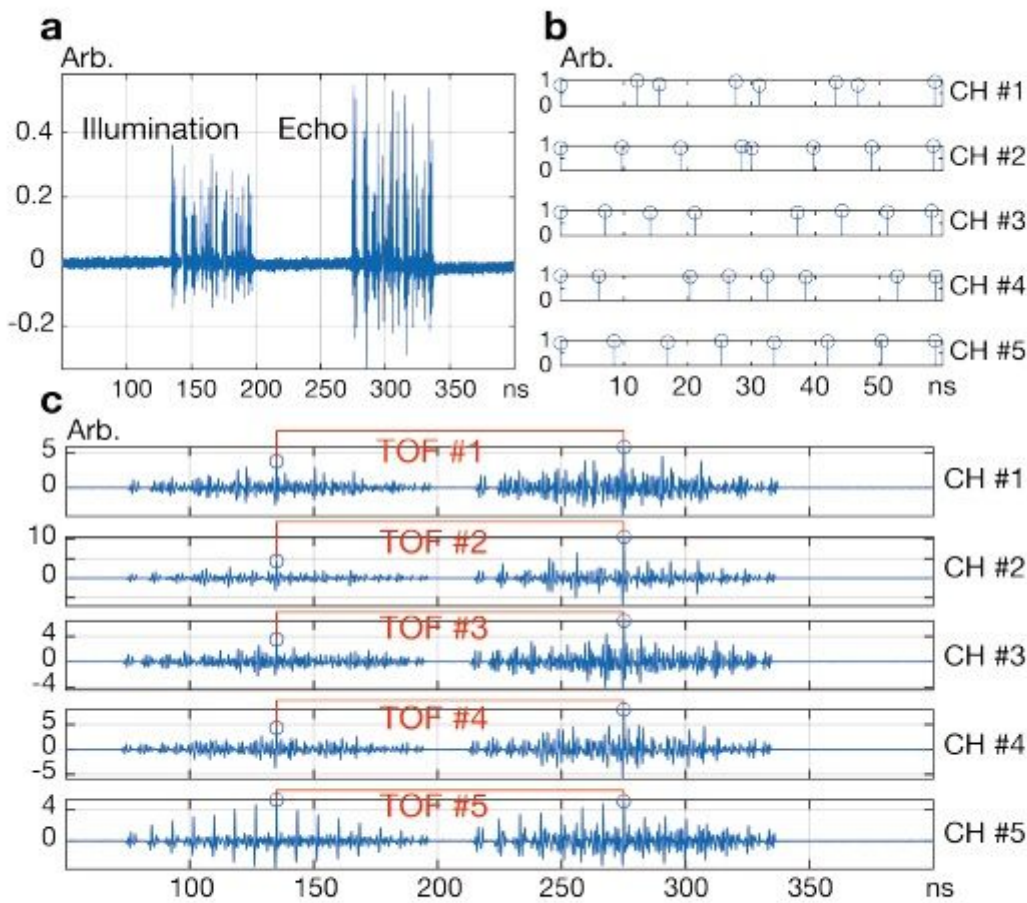


Figure 5

Decoding result. a, sampled echo signal of a parallel group including 5 OOC channels. b, temporal waveform of the 5 OOC codewords. Intensity fluctuations due to fiber optic encoders are incorporated. c, after correlating the echo signal with the 5 OOCs, 5 decoded signals are obtained. Two marked auto-correlation peaks in each decoded channel indicate the transmission time of detection light and the arriving time of echo, respectively.

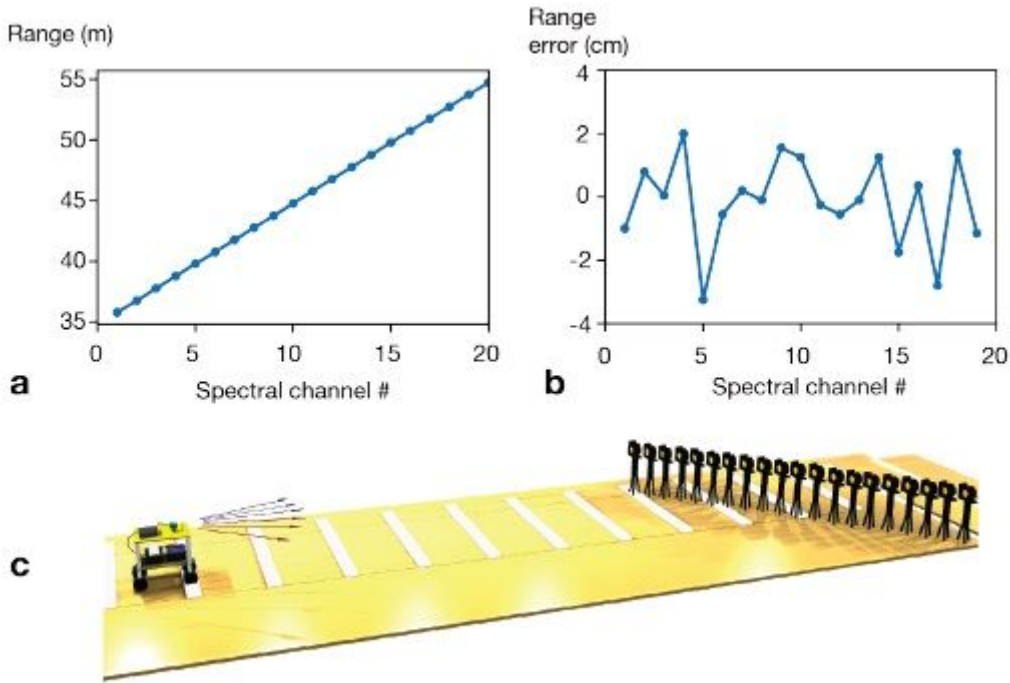


Figure 6

Long-range detection result. a, ranging result of 20 spectral channels. The targets are 20 poles with reflective tags and placed at a range from 21 m to 40 m. The result contains a 14.8-m effective length of fiber link. They are equidistant from each other at a distance of 1 m. b, ranging error of the distance between each adjacent pole, which exhibits a depth resolution of several centimeters. c, experimental setup.

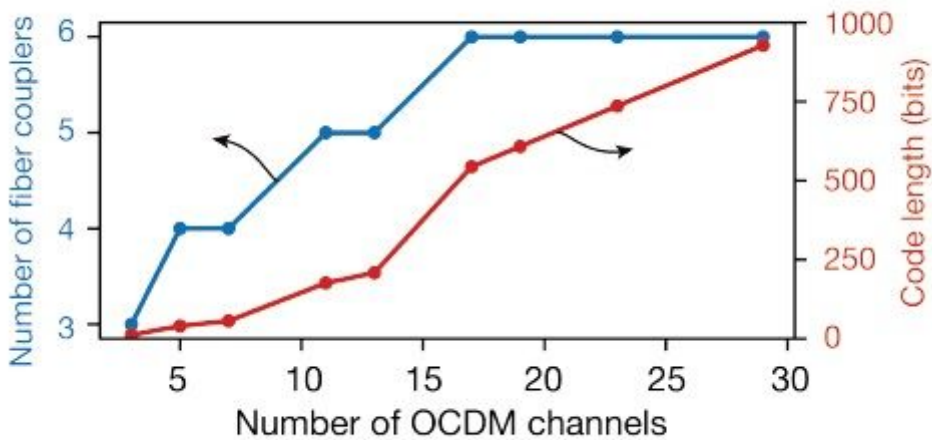


Figure 7

Scalability of OCDM channels using quasi-prime code. As the number of OCDM channels increases, the scale of parallelism increases but code length and the required number of optical couplers per channel

increases as well.

Supplementary Files

This is a list of supplementary files associated with this preprint. Click to download.

- [SupplementaryInformation.pdf](#)